Numerical solutions of a generalized theory for macroscopic capillarity

F. Doster,[1] P. A. Zegeling,[2] and R. Hilfer[1]
[1]*Institut für Computerphysik, Universität Stuttgart, Pfaffenwaldring 27, D-70569 Stuttgart, Germany*
[2]*Department of Mathematics, Faculty of Sciences, Utrecht University, Budapestlaan 6, 3584 TD Utrecht, The Netherlands*
(Received 12 March 2009; revised manuscript received 28 September 2009; published 5 March 2010)

A recent macroscopic theory of biphasic flow in porous media [R. Hilfer, Phys. Rev. E **73**, 016307 (2006)] has proposed to treat microscopically percolating fluid regions differently from microscopically nonpercolating regions. Even in one dimension the theory reduces to an analytically intractable set of ten coupled nonlinear partial differential equations. This paper reports numerical solutions for three different initial and boundary value problems that simulate realistic laboratory experiments. All three simulations concern a closed column containing a homogeneous porous medium filled with two immiscible fluids of different densities. In the first simulation the column is raised from a horizontal to a vertical orientation inducing a buoyancy-driven fluid flow that separates the two fluids. In the second simulation the column is first raised from a horizontal to a vertical orientation and subsequently rotated twice by 180° to compare the resulting stationary saturation profiles. In the third simulation the column is first raised from horizontal to vertical orientation and then returned to its original horizontal orientation. In all three simulations imbibition and drainage processes occur simultaneously inside the column. This distinguishes the results reported here from conventional simulations based on existing theories of biphasic flows. Existing theories are unable to predict flow processes where imbibition and drainage occur simultaneously. The approximate numerical results presented here show the same process dependence and hysteresis as one would expect from an experiment.

DOI: 10.1103/PhysRevE.81.036307 PACS number(s): 47.56.+r, 47.55.−t

I. INTRODUCTION

Although the simultaneous flow of two immiscible and partially wetting fluids inside a porous medium with mixed or variable wettability follows the laws of ordinary hydrodynamics and thermodynamics, the metastable and strongly correlated fluid and interface configurations inside the pore space have resisted theoretical analysis on macroscopic scales for more than a century [1–8]. Darcy's law and its extension to multiphase flow [9–12] are limited to experiments in which the microscopic fluid-fluid interface does not move [13–15].

Multiphase flow phenomena in porous media are of enormous scientific interest and importance in applications ranging from oil recovery [16–18], soil remediation [19], and CO_2 sequestration [20] to paper manufacturing [21] and water management in fuel cells [22]. Although the microscopic flow processes are well understood a macroscopic theory predicting capillary hysteresis and residual fluid distributions remains a highly debated subject [23–27] (see [28–30] for a discussion of this uncommon situation). In fact, the constitutive capillary pressure and relative permeability functions of the accepted Darcy-type theories are difficult to measure [31] and they depend not only on saturation but also on process history [32,33], velocities [34,35], dynamic effects [36,37], interfacial areas [38], flow regimes, and connectivity [39] of the fluids. One tries to cope with these problems by assuming that the extra variables other than saturation can be neglected and one assumes specific parameter functions individually for each displacement process. Recently a different approach was proposed in [29,30,40,41] that eliminates the need to assume capillary pressure functions or relative permeabilities beforehand. Exact and semianalytical solutions of the equations were found in these papers for various special cases. More work on realistic boundary and initial value problems was found necessary to compare the theoretical predictions with experiment.

The purpose of this paper is to propose and solicit experiments by obtaining numerical solutions that allow us to distinguish the extended theory from the traditional theory. For simplicity we focus on one-dimensional profiles and investigate three realistic initial and boundary value problems. These can be realized experimentally using a closed column filled with a homogeneous porous medium and two immiscible fluids. To our knowledge such experiments have not yet been reported in the literature. Our objective is to compute one-dimensional saturation, velocity, and pressure profiles. Using an adaptive grid solver we are able to find approximate numerical profiles that converge to the analytical solution upon refinement.

Given these objectives the paper is structured as follows. Let us begin with a brief review of the underlying theory [29,30,40,42,43] in Sec. II. Once the basic balance laws and constitutive assumptions have been formulated the numerical methods and algorithms to solve the resulting set of coupled nonlinear partial differential equations are presented in Sec. III. Reformulations and adaptations were necessary to cast these equations into a form suitable for a recently developed adaptive moving-grid algorithm [44,45]. It was originally designed to solve conservation laws. A discussion of boundary conditions, initial values, and model parameters is then given in Sec. IV. Model simulations of three experiments on a closed column are finally reported in Sec. V.

All three simulations describe the raising of a closed column in a gravitational field from a horizontal position as proposed and described theoretically in [30]. In the first simulation the column is rotated by 90° from a horizontal to a vertical orientation. In the second simulation the vertically oriented sample is subsequently rotated twice by 180°. In the

third simulation the sample is first rotated by 90° from horizontal to vertical orientation, and then returned back to the original horizontal orientation. The main idea behind these simulations is to illustrate similarities and differences to the standard model. To our knowledge quantitative experimental results for the proposed experiments are currently not available in the literature.

II. MATHEMATICAL MODEL

A. Balance laws

The mathematical model was originally formulated in [29,30,40]. It is based on ideas introduced earlier in [42,43]. The notation and formulation below follows that given in [30]. It was recently extended in [41]. For simplicity, in this paper the discussion will be restricted to one dimension. A one-dimensional porous medium is an appropriate idealization for a column experiment.

Consider immiscible displacement inside a column. The column is idealized as a one-dimensional, homogeneous, isotropic, and incompressible porous medium without isolated pores. Its connected pore space is filled with two incompressible and immiscible fluids, called water and oil. The fluids and the medium are described on length scales much larger than the pore scale. On these length scales a continuum mechanical description in terms of saturation, pressure, and velocity fields applies. The saturations $S_{\mathbb{W}}=S_{\mathbb{W}}(x,t)$ of water and $S_{\mathrm{O}}=S_{\mathrm{O}}(x,t)$ of oil are functions of position $x\in[x_L,x_R]\subset\mathbb{R}$ and time $t\geq 0$.

The key concept of the generalized model is that the percolating (=connected) and the nonpercolating (=not connected) phases have to be treated separately. Following the notation of [30] the percolating phase of water is indexed by $i=1$ and its nonpercolating phase is indexed by $i=2$. The water saturation is then obtained as $S_{\mathbb{W}}=S_1+S_2$. The percolating oil phase is indexed as $i=3$ and its nonpercolating phase is indexed as $i=4$. The oil saturation is defined as $S_{\mathrm{O}}=S_3+S_4$. The volume fraction ϕ_i of phase i is defined as $\phi_i=\phi S_i$, where the porosity ϕ is volume fraction of the pore space. The volume fraction of the solid matrix is denoted as $\phi_5=1-\phi$. Volume conservation requires

$$\phi_1+\phi_2+\phi_3+\phi_4+\phi_5=1, \tag{1a}$$

$$S_1+S_2+S_3+S_4=1, \tag{1b}$$

$$1-\phi=\phi_5 \tag{1c}$$

to hold.

The mass balance of fluid phase i can be expressed in differential form as

$$\frac{\partial(\phi_i\varrho_i)}{\partial t}+\frac{\partial(\phi_i\varrho_i v_i)}{\partial x}=M_i, \tag{2}$$

where $\varrho_i(x,t),\phi_i(x,t),v_i(x,t)$ are mass density, volume fraction, and velocity of phase i as functions of position $x\in[x_L,x_R]$ and time $t\in\mathbb{R}_+$. The quantities M_i denote the mass-transfer rates from all other phases into phase i. The momentum balance is written as $(i=1,2,3,4)$

$$\phi_i\varrho_i\frac{\mathrm{D}^i}{\mathrm{D}t}v_i-\phi_i\frac{\partial\Sigma_i}{\partial x}-\phi_i F_i=m_i-v_i M_i, \tag{3}$$

where Σ_i is the stress tensor in the ith phase, F_i is the body force per unit volume acting on the ith phase, m_i is the momentum transfer into phase i from all the other phases, and $\mathrm{D}^i/\mathrm{D}t=\partial/\partial t+v_i\partial/\partial x$ denotes the material derivative for phase i.

B. Constitutive assumptions

For a macroscopically homogeneous porous medium,

$$\phi(x)=\phi=\text{const} \tag{4}$$

is assumed. Incompressible fluids are assumed so that their densities

$$\varrho_1(x,t)=\varrho_{\mathbb{W}}, \tag{5a}$$

$$\varrho_2(x,t)=\varrho_{\mathbb{W}}, \tag{5b}$$

$$\varrho_3(x,t)=\varrho_{\mathrm{O}}, \tag{5c}$$

$$\varrho_4(x,t)=\varrho_{\mathrm{O}} \tag{5d}$$

are independent of x,t.

The percolating and the nonpercolating phases are able to exchange mass through breakup and coalescence of droplets, ganglia, and clusters. The mass-transfer rates must depend on rates of saturation change. They are assumed here to be

$$M_1=-M_2=\eta_2\phi\varrho_{\mathbb{W}}\left(\frac{S_2-S_2^*}{S_{\mathbb{W}}^*-S_{\mathbb{W}}}\right)\frac{\partial S_{\mathbb{W}}}{\partial t}, \tag{6a}$$

$$M_3=-M_4=\eta_4\phi\varrho_{\mathrm{O}}\left(\frac{S_4-S_4^*}{S_{\mathrm{O}}^*-S_{\mathrm{O}}}\right)\frac{\partial S_{\mathrm{O}}}{\partial t}, \tag{6b}$$

where η_2,η_4 are constants. The parameters $S_{\mathbb{W}}^*,S_{\mathrm{O}}^*,S_2^*,S_4^*$ are defined by

$$S_{\mathbb{W}}^*=(1-S_{\mathrm{Oim}})\Theta(\partial_t S_{\mathbb{W}})+S_{\mathbb{W}\mathrm{dr}}[1-\Theta(\partial_t S_{\mathbb{W}})], \tag{7a}$$

$$S_{\mathrm{O}}^*=1-S_{\mathbb{W}}^*, \tag{7b}$$

$$S_2^*=S_{\mathbb{W}\mathrm{dr}}[1-\Theta(\partial_t S_{\mathbb{W}})], \tag{7c}$$

$$S_4^*=S_{\mathrm{Oim}}\Theta(\partial_t S_{\mathbb{W}}), \tag{7d}$$

where $S_{\mathbb{W}\mathrm{dr}},S_{\mathrm{Oim}}$ are limiting saturations for S_2,S_4. In Eq. (7) the shorthand $\partial_t=\partial/\partial t$ is used and

$$\Theta(x)=\begin{cases}1, & x>0\\ 0, & x\leq 0\end{cases} \tag{8}$$

denotes the Heaviside unit step function. Equation (7) follows from the form used in [29,30] for small rates of saturation change.

Turning to the momentum balance equations, note first that the inertial terms will not be neglected in this paper. The stress tensors for the four phases are specified as

$$\Sigma_1 = -P_1, \tag{9a}$$

$$\Sigma_2 = (-P_3 + \gamma P_2^* S_2^{\gamma-1}), \tag{9b}$$

$$\Sigma_3 = -P_3, \tag{9c}$$

$$\Sigma_4 = (-P_1 + \delta P_4^* S_4^{\delta-1}), \tag{9d}$$

where P_1 and P_3 are the fluid pressures in the percolating phases. The constants P_2^*, P_4^* and exponents γ, δ are constitutive parameters. They can be determined experimentally from capillary pressure functions and may have very different magnitudes. The pressure for the nonpercolating phases is changed as compared to the ambient pressure of the surrounding phase. This phenomenon was anticipated in [29,30] and seems indeed to have recently been observed in experiment [46]. The macroscopic body forces are assumed to be given by gravity and capillarity. They are specified as

$$F_1 = \varrho_1 g \sin\vartheta, \tag{10a}$$

$$F_2 = \varrho_2 g \sin\vartheta + \Pi_a \frac{\partial S_1^{-\alpha}}{\partial x}, \tag{10b}$$

$$F_3 = \varrho_3 g \sin\vartheta, \tag{10c}$$

$$F_4 = \varrho_4 g \sin\vartheta + \Pi_b \frac{\partial S_3^{-\beta}}{\partial x}, \tag{10d}$$

with constitutive constants Π_a, Π_b and exponents α, $\beta > 0$. Note that capillary body forces do not exist on the pore scale, but appear only in the coarse graining from pore to macroscale. Again, these parameters can be determined experimentally. The angle $0 \le \vartheta \le \pi/2$ is the angle between the direction of the column and the direction of gravity with $\vartheta = \pi/2$ corresponding to alignment. Finally, the momentum-transfer terms are assumed to be given by linear viscous drag characterized by constitutive resistance coefficients R_{ij} through the equations

$$m_1 = R_{13}(v_3 - v_1) + R_{14}(v_4 - v_1) - R_{15}v_1, \tag{11a}$$

$$m_2 = R_{23}(v_3 - v_2) + R_{24}(v_4 - v_2) - R_{25}v_2, \tag{11b}$$

$$m_3 = R_{31}(v_1 - v_3) + R_{32}(v_2 - v_3) - R_{35}v_3, \tag{11c}$$

$$m_4 = R_{41}(v_1 - v_4) + R_{42}(v_2 - v_4) - R_{45}v_4, \tag{11d}$$

where $R_{12}=0$ and $R_{34}=0$ were used because there is no common interface and hence no direct viscous interaction between these phase pairs. Remember that the index $i=5$ represents the rock matrix. For more details on these constitutive assumptions the reader is referred to the original papers [29,30,40].

The balance laws (1b), (2), and (3) combined with the constitutive assumptions given above provide nine equations for the ten unknowns S_i, v_i, P_1, P_3 with $i=1,2,3,4$. To close the system of equations the condition $v_2=0$ or $v_4=0$ could be used. These conditions apply when the nonpercolating phases are immobile as it is often observed in experiment. It turns out, however, that there exists a less restrictive and, in our opinion, more natural self-consistent closure.

The self-consistent closure condition used in this paper follows naturally from many limiting cases [56]. One such a limit is the residual decoupling approximation close to hydrostatic equilibrium described in detail and utilized in ([30], Sec. 5, p. 216). A second more general limiting case is the limit of vanishing velocities, i.e., $v_i \to 0$ for $i=1,2,3,4$. Following [56], we formulate the self-consistent closure condition in its most general form as

$$\begin{aligned} 0 = &\left(\frac{R_{13}}{\phi_1} + \frac{R_{14}}{\phi_1} + \frac{R_{15}}{\phi_1} + \frac{R_{31}}{\phi_3} - \frac{R_{41}}{\phi_4} + \frac{M_1}{\phi_1}\right)v_1 + \varrho_1 \frac{\mathrm{D}^1}{\mathrm{D}t} v_1 \\ &+ \left(-\frac{R_{23}}{\phi_2} - \frac{R_{24}}{\phi_2} - \frac{R_{25}}{\phi_2} + \frac{R_{32}}{\phi_3} - \frac{R_{42}}{\phi_4} + \frac{M_1}{\phi_2}\right)v_2 - \varrho_2 \frac{\mathrm{D}^2}{\mathrm{D}t} v_2 \\ &+ \left(-\frac{R_{13}}{\phi_1} + \frac{R_{23}}{\phi_2} - \frac{R_{31}}{\phi_3} - \frac{R_{32}}{\phi_3} - \frac{R_{35}}{\phi_3} - \frac{M_3}{\phi_3}\right)v_3 - \varrho_3 \frac{\mathrm{D}^3}{\mathrm{D}t} v_3 \\ &+ \left(-\frac{R_{14}}{\phi_1} + \frac{R_{24}}{\phi_2} + \frac{R_{41}}{\phi_4} + \frac{R_{42}}{\phi_4} + \frac{R_{45}}{\phi_4} - \frac{M_3}{\phi_4}\right)v_4 + \varrho_4 \frac{\mathrm{D}^4}{\mathrm{D}t} v_4. \end{aligned} \tag{12}$$

This condition follows self-consistently from the constitutive theory. It expresses the experimental observation that the pressure difference $P_3 - P_1$ depends more strongly on saturations than on velocities, and that it remains nonzero even for vanishing velocities. Adding Eq. (3) for $i=2$ and 3 and subtracting Eq. (3) with $i=1$ and 4 from the result gives

$$\frac{\partial P_3}{\partial x} = \frac{\partial P_1}{\partial x} + \frac{1}{2}\frac{\partial}{\partial x}(\Pi_a S_1^{-\alpha} - \Pi_b S_3^{-\beta} + \gamma P_2^* S_2^{\gamma-1} - \delta P_4^* S_4^{\delta-1}). \tag{13}$$

In this form the self-consistent closure has been used in the numerical calculation below.

III. NUMERICAL IMPLEMENTATION

A. Adaptive moving-grid technique

The coupled system of nonlinear partial differential and algebraic equations is solved numerically using an adaptive moving-grid solver [44,45]. Its original FORTRAN implementation was described in [44] and we follow their notation. Space is discretized by finite differences on a nonuniformly distributed grid. The time integration within this algorithm is performed using the public domain solver DASSL [47], which is an implicit time-integration module with variable order ranging from first to fifth and variable time steps. The first-order variant reduces to the implicit backward Euler scheme, while the higher-order integrators follow the backward-differentiation-formula approach. The system of N_{PDE} partial differential equations is generally formulated as

$$C\left(x,t,\mathbf{u},\frac{\partial \mathbf{u}}{\partial x}\right)\frac{\partial \mathbf{u}}{\partial t}+\mathbf{Q}\left(x,t,\mathbf{u},\frac{\partial \mathbf{u}}{\partial x}\right)=\frac{\partial}{\partial x}\left[\mathbf{R}\left(x,t,\mathbf{u},\frac{\partial \mathbf{u}}{\partial x}\right)\right], \tag{14}$$

where C is a $N_{\mathrm{PDE}}\times N_{\mathrm{PDE}}$ matrix, $x\in[x_L,x_R]\subset\mathbb{R}$, $t>t_0$, and $\mathbf{u}=(u_1,\ldots,u_{N_{\mathrm{PDE}}})^T$ is the vector of unknowns. The vectors $\mathbf{Q}$ and $\mathbf{R}$ are both of length N_{PDE}. They represent sinks and flux terms.

The boundary conditions in the code are formulated in the form

$$B_j(x,t)R_j=\tilde{\Gamma}_j\left(x,t,\mathbf{u},\frac{\partial \mathbf{u}}{\partial x},\frac{\partial \mathbf{u}}{\partial t}\right)+\Gamma_j\left(x,t,\mathbf{u},\frac{\partial \mathbf{u}}{\partial x}\right), \tag{15}$$

for $j=1,\ldots,N_{\mathrm{PDE}}$, where R_j is the jth component of the vector $\mathbf{R}$. All functions R_j, B_j, $\tilde{\Gamma}_j$, and Γ_j are then evaluated at $x=x_L$ (left boundary) and $x=x_R$ (right boundary). The initial conditions are specified as

$$\mathbf{u}(x,t_0)=\mathbf{u}^0(x), \tag{16}$$

for $x\in[x_L,x_R]$.

The user of the code has to define the matrix C, the vectors $\mathbf{Q}$ and $\mathbf{R}$, and the functions B_j, $\tilde{\Gamma}_j$, Γ_j, and $\mathbf{u}^0$. Also, the accuracy of the time-integration method in DASSL must be specified by a parameter ϵ_{tol} [47]. An additional feature of the code is the option to let the numerical grid automatically adapt itself during the time integration to the changing spatial profiles of the different components of $\mathbf{u}$. The main idea behind the adaptivity procedure is the equidistribution principle. In its pure form the principle states that $\Delta x_i\omega_i=\mathrm{const}$, where the function ω is monitoring the spatial derivatives of the vector $\mathbf{u}$. This means that low values of ω would result in wider grid cells Δx_i, whereas higher values of ω, stressing regions in the solution with higher spatial activity, gives more closely spaced grid cells. The equidistribution principle holds because the integral of the monitor function ω over each grid cell $[x_{i-1},x_i]$ equals the average value of the monitor function over the whole interval $[x_L,x_R]$. The latter quantity can be expressed in terms of the total integral of ω divided by the number grid points. As a result of this, after approximating the integrals, the product of Δx_i and ω_i can be kept constant for all time $t\geq t_0$. The pure equidistribution principle for a nonuniform grid is obtained by switching off two smoothing parameters (named τ_S and σ_s) in the code. The reader who is interested in more details is referred to [44,48].

It must be noted—as is shown in earlier work, for example, in [49,50]—that adaptive grids using this basic principle may become oscillatory in the time direction and rather irregularly distributed in the spatial direction. This would lead to severe numerical problems for the time-integration scheme and finally also to a great loss of accuracy. In many cases it can even result in a complete breakdown of the computation. To prevent this from happening, two smoothing procedures were added to the basic algorithm: one in the time direction and the other in the spatial direction. The main effect of the smoothing is that the spatial grid lines become free from unwanted oscillations as a function of time (if $\tau_s>0$) and that the nonuniform grid is always "nicely" distributed (if $\sigma_s>0$). This last effect can be formulated as

$$\frac{\sigma_s}{\sigma_s+1}\leq\frac{\Delta x_{i+1}}{\Delta x_i}\leq\frac{\sigma_s+1}{\sigma_s}, \tag{17}$$

for all i and for all $t\geq t_0$. Typical values for the two parameters in the numerical experiments are $\tau_s=T/1000$ and $\sigma_s=2$, where T denotes the length of the time interval of interest. An extra improvement, compared to the original code as described in [44], was recently made to the adaptive grid code. During the time integration, the monitor function ω, in which the spatial derivatives of $\mathbf{u}$ play a crucial role, must remain positive because otherwise the calculated nonuniform grid may collapse during the time integration, i.e., the step size may become infinitesimally small. Obviously, this would lead to a breakdown in the computations. Introducing a regularization parameter $\alpha_c>0$, as is done in [44], guarantees the positivity of the function ω. However, this parameter α_c was chosen to be fixed in time and, unfortunately, depends on the scales of both $\mathbf{u}$ and x. Making this parameter "adaptive" as well and time dependent, as is done in [45,48], serves to increase the user friendliness of the adaptive code. We have used this improved version of the adaptive grid code for the numerical simulations.

B. Model reformulation and approximation

The mathematical model proposed in Sec. II does not fit exactly to the structure of the solver. Reformulations and adaptations are necessary. The equations are

$$\frac{\partial S_1}{\partial t}+\frac{\partial(S_1v_1)}{\partial x}=\eta_2\left(\frac{S_2-S_2^*}{S_{\mathbb{W}}^*-S_{\mathbb{W}}}\right)\frac{\partial S_{\mathbb{W}}}{\partial t}, \tag{18a}$$

$$\frac{\partial S_2}{\partial t}+\frac{\partial(S_2v_2)}{\partial x}=-\eta_2\left(\frac{S_2-S_2^*}{S_{\mathbb{W}}^*-S_{\mathbb{W}}}\right)\frac{\partial S_{\mathbb{W}}}{\partial t}, \tag{18b}$$

$$\frac{\partial S_3}{\partial t}+\frac{\partial(S_3v_3)}{\partial x}=\eta_4\left(\frac{S_4-S_4^*}{S_{\mathrm{O}}^*-S_{\mathrm{O}}}\right)\frac{\partial S_{\mathrm{O}}}{\partial t}, \tag{18c}$$

$$\frac{\partial S_4}{\partial t}+\frac{\partial(S_4v_4)}{\partial x}=-\eta_4\left(\frac{S_4-S_4^*}{S_{\mathrm{O}}^*-S_{\mathrm{O}}}\right)\frac{\partial S_{\mathrm{O}}}{\partial t}, \tag{18d}$$

$$\varrho_{\mathbb{W}}\frac{\mathrm{D}^1}{\mathrm{D}t}v_1+\frac{\partial P_1}{\partial x}-\varrho_{\mathbb{W}}g\sin\vartheta=\sum_{j=1}^{5}\frac{R_{1j}}{\phi S_1}(v_j-v_1)-\frac{\eta_2v_1\varrho_{\mathbb{W}}}{S_1}\left(\frac{S_2-S_2^*}{S_{\mathbb{W}}^*-S_{\mathbb{W}}}\right)\frac{\partial S_{\mathbb{W}}}{\partial t}, \tag{18e}$$

$$\varrho_{\mathbb{W}}\frac{\mathrm{D}^2}{\mathrm{D}t}v_2+\frac{\partial}{\partial x}(P_3-\gamma P_2^*S_2^{\gamma-1}-\Pi_aS_1^{-\alpha})-\varrho_{\mathbb{W}}g\sin\vartheta=\sum_{j=1}^{5}\frac{R_{2j}}{\phi S_2}(v_j-v_2)+\frac{\eta_2v_2\varrho_{\mathbb{W}}}{S_2}\left(\frac{S_2-S_2^*}{S_{\mathbb{W}}^*-S_{\mathbb{W}}}\right)\frac{\partial S_{\mathbb{W}}}{\partial t}, \tag{18f}$$

$$\varrho_{\mathrm{O}}\frac{\mathrm{D}^3}{\mathrm{D}t}v_3+\frac{\partial P_3}{\partial x}-\varrho_{\mathrm{O}}g\sin\vartheta=\sum_{j=1}^{5}\frac{R_{3j}}{\phi S_3}(v_j-v_3)-\frac{\eta_4 v_3\varrho_{\mathrm{O}}}{S_3}\left(\frac{S_4-S_4^*}{S_{\mathrm{O}}^*-S_{\mathrm{O}}}\right)\frac{\partial S_{\mathrm{O}}}{\partial t},\tag{18g}$$

$$\varrho_{\mathrm{O}}\frac{\mathrm{D}^4}{\mathrm{D}t}v_4+\frac{\partial}{\partial x}(P_1-\delta P_4^* S_4^{\delta-1}-\Pi_{\mathrm{b}}S_3^{-\beta})-\varrho_{\mathbb{W}}g\sin\vartheta=\sum_{j=1}^{5}\frac{R_{4j}}{\phi S_4}(v_j-v_4)+\frac{\eta_4 v_4\varrho_{\mathrm{O}}}{S_4}\left(\frac{S_4-S_4^*}{S_{\mathrm{O}}^*-S_{\mathrm{O}}}\right)\frac{\partial S_{\mathrm{O}}}{\partial t},\tag{18h}$$

$$S_1+S_2+S_3+S_4=1,\tag{18i}$$

$$\frac{\partial P_3}{\partial x}=\frac{\partial P_1}{\partial x}+\frac{1}{2}\frac{\partial}{\partial x}(\Pi_{\mathrm{a}}S_1^{-\alpha}-\Pi_{\mathrm{b}}S_3^{-\beta}+\gamma P_2^* S_2^{\gamma-1}-\delta P_4^* S_4^{\delta-1}),\tag{18j}$$

where $v_5=0$, $R_{12}=0$, $R_{21}=0$, $R_{34}=0$, $R_{43}=0$ and the quantities $S_{\mathbb{W}}^*, S_{\mathrm{O}}^*, S_2^*, S_4^*$ are defined in Eq. (7).

1. Identification of primary unknowns

Set (18) of ten coupled nonlinear partial differential equations is reduced to nine equations by inserting Eq. (18j) into Eqs. (18f) and (18g) to eliminate $\partial P_3/\partial x$. The remaining nine unknowns are identified as $u_1=S_1$, $u_2=S_2$, $u_3=S_3$, $u_4=S_4$, $u_5=v_1$, $u_6=v_2$, $u_7=v_3$, $u_8=v_4$, $u_9=P_1$. Equations (18) are numbered from $i=1$ for Eq. (18a) to $i=N_{\mathrm{PDE}}=9$ for Eq. (18i).

2. Time derivatives

The time derivatives $\partial S_{\mathbb{W}}/\partial t$ and $\partial S_{\mathrm{O}}/\partial t$ can be expressed by spatial derivatives as follows:

$$\frac{\partial S_{\mathbb{W}}}{\partial t}=-\frac{\partial S_{\mathrm{O}}}{\partial t}=-\frac{\partial}{\partial x}(S_1 v_1+S_2 v_2).\tag{19}$$

The first equality follows from the volume conservation $S_{\mathbb{W}}+S_{\mathrm{O}}=1$ and the second is obtained by adding Eqs. (18a) and (18b). By this means the nonlinear terms in Eq. (7) can be treated and also the treatment of the time derivatives in the mass-exchange terms (6) is facilitated.

3. Regularization of saturation

The numerical solver does not respect the condition $S_i>0$ during iterations. To avoid overflows and complex numbers the saturations have to be bounded away from zero. This is achieved by replacing every occurrence of S_i with

$$S_i(x,t)\to\max(S_i(x,t),\epsilon_S),\tag{20}$$

where ϵ_S is a small regularization parameter.

4. Flux symmetrization

Experience has shown that the algorithm performs better if the mass fluxes are symmetrized. Therefore, the mass flux $S_i v_i$ of phase i is replaced with

$$S_i v_i=\frac{1}{2}\left(S_i v_i-\sum_{\substack{j=1\\ j\neq i}}^{4}S_j v_j\right)\tag{21}$$

wherever it occurs.

5. Fluxes as sources

Tests have shown that the stability and computation time is substantially improved if first-order spatial derivatives are identified as source terms and assigned into the vector **Q** rather than as flux terms associated with the vector **R** in Eq. (14). Therefore, first-order spatial derivatives were included into **Q**.

6. Volume conservation and pressure stabilization

The volume conservation (18i) is an algebraic equation and could be used to eliminate one of the saturations. This is done frequently in numerical schemes for the traditional theory [51,52]. It is not done here because the incompressibility of the fluids results in the absence of an equation for the time evolution of the pressure and Eq. (18i) is a natural candidate to remedy this situation. Solving Eq. (18i) and eliminating a saturation would eliminate this equation and with it the possibility to view it as an equation for $P_1=u_9$.

To turn Eq. (18i) into a partial differential equation related to incompressibility of the fluids it is first differentiated with respect to time to obtain

$$\frac{\partial}{\partial t}(S_1+S_2+S_3+S_4)=0.\tag{22}$$

Next, using the mass balances to replace $\partial_t S_i$, this equation can be transformed into a partial differential equation without time derivatives,

$$\frac{\partial}{\partial x}(S_1 v_1+S_2 v_2+S_3 v_3+S_4 v_4)=0.\tag{23}$$

This equation becomes the pressure equation by adding an artificial second-order term for the pressure

$$\frac{\partial}{\partial x}(S_1 v_1+S_2 v_2+S_3 v_3+S_4 v_4)=\epsilon_P\frac{\partial^2 u_9}{\partial x^2},\tag{24}$$

where $\epsilon_P\approx 0$ is a small artificial numerical parameter. This is a well-known method for numerical treatment of the incompressible Navier-Stokes equation and is there called the pressure stabilization or pressure projection method [53–55]. The influence of the artificial parameter has been checked and beside the stabilization no change in the solution is seen for 10^{-20} m^3 s kg$^{-1}<\epsilon_P<10^{-14}$ m^3 s kg^{-1}.

C. Model implementation and numerical parameters

With these preparations the model can be cast into the form of Eq. (14). The parameters and parameter functions are chosen as follows: the time evolution matrix C is diagonal,

$$C=\mathrm{diag}(1,1,1,1,1,1,1,1,0).\tag{25}$$

The elements of the source vector **Q** for equation $i=1,\ldots,4$ (mass balances) are

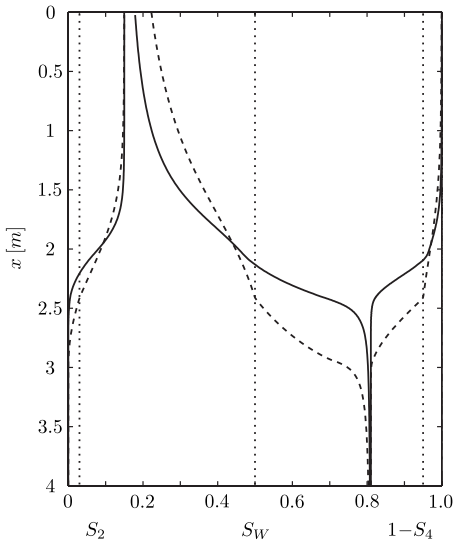

FIG. 1. Stationary saturation profiles $S_2(x)$, $S_{\mathbb{W}}(x)$, and $1-S_4(x)$ functions of x reached after $t=150\tau_r$ (shown as solid lines). The dashed lines are the quasistatic profiles obtained in ([30], Fig. 6). The initial conditions are shown as dotted lines.

$$Q_i = \frac{1}{2}\left[u_i \frac{\partial u_{i+4}}{\partial x} + u_{i+4}\frac{\partial u_i}{\partial x} - \sum_{\substack{j=1 \\ j\neq i}}^{4} \left(u_j \frac{\partial u_{j+4}}{\partial x} + u_{j+4}\frac{\partial u_j}{\partial x} \right) \right] - \tilde{M}_i \tag{26}$$

with, e.g., for $i=1$,

$$\tilde{M}_1 = -\eta_2 \frac{u_2 - S_2^* \Theta\left[-\sum_{i=1}^{2} \left(u_i \frac{\partial u_{i+4}}{\partial x} + u_{i+4}\frac{\partial u_i}{\partial x} \right) \right]}{S_{\mathbb{W}}^* \Theta\left[-\sum_{i=1}^{2} \left(u_i \frac{\partial u_{i+4}}{\partial x} + u_{i+4}\frac{\partial u_i}{\partial x} \right) \right] - u_1 - u_2} \times \sum_{i=1}^{2} \left(u_i \frac{\partial u_{i+4}}{\partial x} + u_{i+4}\frac{\partial u_i}{\partial x} \right). \tag{27}$$

The elements for the momentum balance, e.g., of the percolating water phase ($i=5$) are

$$Q_5 = \frac{1}{\phi \varrho_{\mathbb{W}} u_1}[(R_{15}+R_{12}+R_{13}+R_{14})u_5 - R_{12}u_6 - R_{13}u_7 - R_{14}u_8] + \frac{u_5}{u_1}\tilde{M}_1 + \frac{1}{\varrho_{\mathbb{W}}}\frac{\partial u_9}{\partial x} + u_5 \frac{\partial u_5}{\partial x} - g \sin\vartheta. \tag{28}$$

The elements of the source vector Q_i of the remaining momentum balances ($i=6,7,8$) are formulated similarly. The source vector element for the pressure equation is

$$Q_9 = \sum_{i=1}^{4} \left(u_i \frac{\partial u_{i+4}}{\partial x} + u_{i+4}\frac{\partial u_i}{\partial x} \right). \tag{29}$$

The flux vector contains only the artificial numerical parameter for the pressure,

TABLE I. Numerical parameters used for all simulations.

Parameter	Value
n_{pts}	51
τ_s	5.0
σ_s	2.0
ϵ_{tol}	10^{-5}
ϵ_P	10^{-18} m^3 s/kg
ϵ_S	10^{-5}

$$\mathbf{R} = (0,0,0,0,0,0,0,0,\epsilon_P)^T. \tag{30}$$

For convenience the numerical parameters are summarized in Table I.

IV. INITIAL CONDITIONS, BOUNDARY CONDITIONS, AND SIMULATION PARAMETERS

A. Boundary conditions

Within this work we present numerical simulations of three laboratory experiments. All of them are carried out with a column containing a homogeneous porous medium. Its pore space is filled with oil and water. It has impermeable walls on all sides and hence its boundary conditions in one dimension are expressed mathematically as

$$v_i(x_L,t) = 0, \tag{31}$$

$$v_i(x_R,t) = 0, \tag{32}$$

for $i=1,\ldots,4$. Due to the incompressibility of the fluids, the pressure has to be fixed at one point, e.g., the left boundary,

$$P_1(x_L,t) = 0. \tag{33}$$

In the algorithm, the boundary conditions are specified through the three vectors $B(x,t)$, $\Gamma(x,t,\mathbf{u}(x,t),\partial_x\mathbf{u}|_x)$, and $\tilde{\Gamma}(x,t,\mathbf{u}(x,t),\partial_x\mathbf{u}|_x,\partial_t\mathbf{u}|_x)$ on both sides $x\in(x_L,x_R)$. Rewriting the boundary conditions (31)–(33) in this form results in

$$\mathbf{B}(x_L,t) = (0,0,0,0,0,0,0,0,0)^T, \tag{34a}$$

$$\mathbf{B}(x_R,t) = (0,0,0,0,0,0,0,0,0)^T, \tag{34b}$$

for the vector corresponding to flux boundary conditions, and

$$\Gamma(x_L,t,\mathbf{u}(x_L,t),\partial_x\mathbf{u}|_{x=x_L}) = (0,0,0,0,u_5(x_L,t),u_6(x_L,t),u_7(x_L,t),u_8(x_L,t),u_9(x_L,t))^T, \tag{35a}$$

$$\Gamma(x_R,t,\mathbf{u}(x_R,t),\partial_x\mathbf{u}|_{x=x_R}) = (0,0,0,0,u_5(x_R,t),u_6(x_R,t),u_7(x_R,t),u_8(x_R,t),0)^T, \tag{35b}$$

for the vector corresponding to Dirichlet and von Neumann boundary conditions. When there is no boundary condition specified the equations of motion themselves are solved at the boundary. At the left boundary this leads to

$$\tilde{\Gamma}_i(x_L,t,\mathbf{u}(x_L,t),\partial_x\mathbf{u}|_{x=x_L},\partial_t\mathbf{u}|_{x=x_L}) = \left.\frac{\partial u_i}{\partial t}\right|_{x=x_L} + \frac{1}{2}\left[u_i(x_L,t)\left.\frac{\partial u_{i+4}}{\partial x}\right|_{x=x_L} + u_{i+4}(x_L,t)\left.\frac{\partial u_i}{\partial x}\right|_{x=x_L} - \sum_{\substack{j=1\\ j\neq i}}^{4}\left(u_j(x_L,t)\left.\frac{\partial u_{j+4}}{\partial x}\right|_{x=x_L} + u_{j+4}(x_L,t)\left.\frac{\partial u_j}{\partial x}\right|_{x=x_L}\right)\right] - \tilde{M}_i(x_L,t), \tag{36a}$$

for $i=1,3$; to

$$\tilde{\Gamma}_i(x_L,t,\mathbf{u}(x_L,t),\partial_x\mathbf{u}|_{x=x_L},\partial_t\mathbf{u}|_{x=x_L}) = \left.\frac{\partial u_i}{\partial t}\right|_{x=x_L} + u_i(x_L,t)\left.\frac{\partial u_{i+4}}{\partial x}\right|_{x=x_L} + u_{i+4}(x_L,t)\left.\frac{\partial u_i}{\partial x}\right|_{x=x_L} + \tilde{M}_{i-1}(x_L,t), \tag{36b}$$

for $i=2,4$; and to

$$\tilde{\Gamma}_i(x_L,t,\mathbf{u}(x_L,t),\partial_x\mathbf{u}|_{x=x_L},\partial_t\mathbf{u}|_{x=x_L}) = 0, \tag{36c}$$

for $i=5,\ldots,9$. At the right boundary it leads to

$$\tilde{\Gamma}_i(x_R,t,\mathbf{u}(x_R,t),\partial_x\mathbf{u}|_{x=x_R},\partial_t\mathbf{u}|_{x=x_R}) = \left.\frac{\partial u_i}{\partial t}\right|_{x=x_R} + \frac{1}{2}\left[u_i(x_R,t)\left.\frac{\partial u_{i+4}}{\partial x}\right|_{x=x_R} + u_{i+4}(x_R,t)\left.\frac{\partial u_i}{\partial x}\right|_{x=x_R} - \sum_{\substack{j=1\\ j\neq i}}^{4}\left(u_j(x_R,t)\left.\frac{\partial u_{j+4}}{\partial x}\right|_{x=x_R} + u_{j+4}(x_R,t)\left.\frac{\partial u_j}{\partial x}\right|_{x=x_R}\right)\right] - \tilde{M}_i(x_R,t), \tag{37a}$$

for $i=1,3$; to

$$\tilde{\Gamma}_i(x_R,t,\mathbf{u}(x_R,t),\partial_x\mathbf{u}|_{x=x_R},\partial_t\mathbf{u}|_{x=x_R}) = \left.\frac{\partial u_i}{\partial t}\right|_{x=x_R} + u_i(x_R,t)\left.\frac{\partial u_{i+4}}{\partial x}\right|_{x=x_R} + u_{i+4}(x_R,t)\left.\frac{\partial u_i}{\partial x}\right|_{x=x_R} + \tilde{M}_{i-1}(x_R,t), \tag{37b}$$

for $i=2,4$; to

$$\tilde{\Gamma}_i(x_R,t,\mathbf{u}(x_R,t),\partial_x\mathbf{u}|_{x=x_R},\partial_t\mathbf{u}|_{x=x_R}) = 0, \tag{37c}$$

for $i=5,\ldots,8$; and to

$$\tilde{\Gamma}_9(x_R,t,\mathbf{u}(x_R,t),\partial_x\mathbf{u}|_{x=x_R},\partial_t\mathbf{u}|_{x=x_R}) = \sum_{j=1}^{4}\left(u_j(x_R,t)\left.\frac{\partial u_{j+4}}{\partial x}\right|_{x=x_R} + u_{j+4}(x_R,t)\left.\frac{\partial u_j}{\partial x}\right|_{x=x_R}\right), \tag{37d}$$

for $i=9$. Note that here the symmetrization (21) was not used for the nonpercolating phases. This contributes to a further reduction in numerical oscillations.

B. Initial conditions

The three simulations differ in the initial conditions. Initial condition A is taken from [30]. Initial condition B corresponds to a situation after primary imbibition where 50% of the pore space is filled with water. Initial condition C represents a situation where 50% of the pore space is filled with water after primary drainage. Initial condition D models a situation with 30% water after primary imbibition and initial condition E models one with 30% water after primary drainage. For the initial conditions B–E the residual decoupling approximation is used to calculate the amount of percolating and nonpercolating phases. The different initial conditions are summarized in Table II.

TABLE II. The five different initial conditions for which the equations are solved. In the initial conditions A–C 50% of the pore volume of the column is filled with water and 50% with oil. In initial conditions D and E 30% are filled with water and 70% with oil.

	A	B	C	D	E
$u_1^0(x)$	0.450	0.499	0.354	0.299	0.151
$u_2^0(x)$	0.050	0.001	0.146	0.001	0.149
$u_3^0(x)$	0.470	0.321	0.499	0.557	0.699
$u_4^0(x)$	0.030	0.179	0.001	0.143	0.001
$u_5^0(x)$	0.0	0.0	0.0	0.0	0.0
$u_6^0(x)$	0.0	0.0	0.0	0.0	0.0
$u_7^0(x)$	0.0	0.0	0.0	0.0	0.0
$u_8^0(x)$	0.0	0.0	0.0	0.0	0.0
$u_9^0(x)$	0.0	0.0	0.0	0.0	0.0

C. Simulation parameters

The fluid, rock, and column properties are taken from [30]. These are $\phi=0.34$, $S_{\mathbb{W}\mathrm{dr}}=0.15$, $S_{\mathbb{O}\mathrm{im}}=0.19$, $\eta_2=4$, $\eta_4=3$, $\varrho_{\mathbb{W}}=1000$ kg m^{-3}, $\varrho_{\mathbb{O}}=800$ kg m^{-3}, $\alpha=0.52$, $\beta=0.90$, $\gamma=1.5$, $\delta=3.5$, $\Pi_a=1620$ Pa, $\Pi_b=25$ Pa, $P_2^*=2500$ Pa, $P_4^*=400$ Pa, $x_L=0$ m, and $x_R=4$ m. Values for the resistance coefficients were not given or needed in [30], because only stationary solutions were addressed there. To obtain realistic time scales the resistance coefficients are chosen in a way that the maximum values of the relative permeabilities, which can be identified in the residual decoupling approximation, are $\mathcal{O}(1)$.

This leads to

$$R_1 = \frac{2\mu_{\mathbb{W}}\phi^2}{k}, \tag{38a}$$

$$R_3 = \frac{2\mu_{\mathbb{O}}\phi^2}{k}, \tag{38b}$$

with the abbreviations $R_1=R_{13}+R_{14}+R_{15}$ and $R_3=R_{31}+R_{32}+R_{35}$. Realistic values for the viscosities are $\mu_{\mathbb{W}}=0.001$ kg m^{-1} s^{-1} and $\mu_{\mathbb{O}}=0.001$ kg m^{-1} s^{-1} and for the permeability $k=1\times10^{-12}$ m^2 (e.g., [52]). Assuming that the coupling is of the same magnitude for all the viscous couplings of the percolating phases, one obtains $R_{15}=R_{13}$

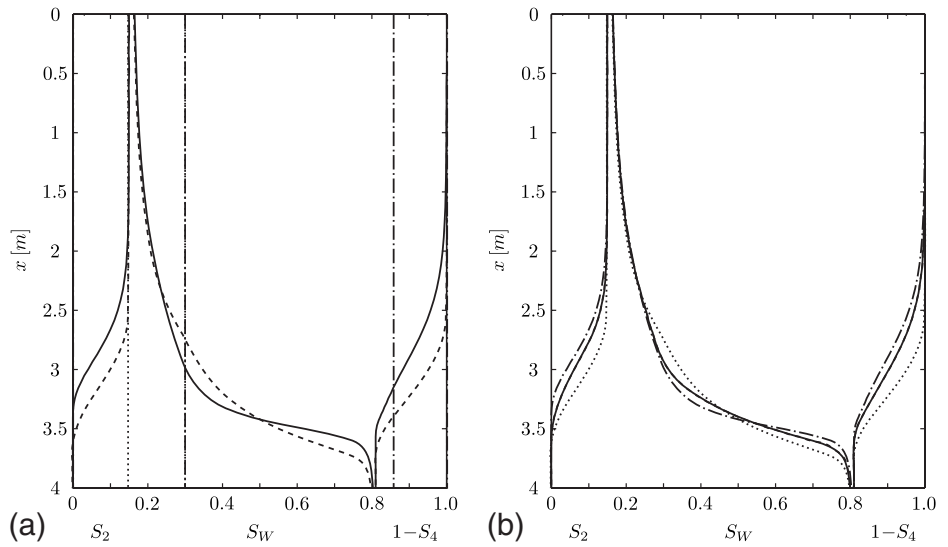

FIG. 2. Stationary saturation profiles and initial conditions for simulation 2. (a) shows the profiles after raising the column from horizontal to vertical position, while (b) shows the stationary profiles at the end of simulation 2. Solid curves represent saturation profiles corresponding to initial conditions D and dashed curves correspond to initial conditions E. The dashed curves in (b) are not visible because they coincide with the solid curves. In (a) initial saturation profiles for case D are shown as dashed-dotted vertical lines and for case E as dotted lines. In (b) the dashed-dotted curves are identical to the solid curves in (a). The dotted curves in (b) are identical to the dashed curves in (a). In (a) there is a dashed-dotted vertical line at $S_2=0.001$, a dotted vertical line at $1-S_4=0.999$, and the vertical line at $S_{\mathbb{W}}=0.3$ is a superposition of a dotted and a dashed-dotted line.

$=R_{14}=0.77\times10^8$ kg m^{-3} s^{-1} and $R_{35}=R_{31}=R_{32}=0.77\times10^8$ kg m^{-3} s^{-1}. For the viscous coupling terms between the nonpercolating phases and the soil, R_{25} and R_{45}, no measurements or estimates are available so far. It seems reasonable to assume that these resistances are much larger than the viscous resistances of the percolating phases R_{15} and R_{35}. Specifically, $R_{25}=10^{16}$ kg m^{-3} s^{-1} and $R_{45}=10^{16}$ kg m^{-3} s^{-1} are chosen in subsequent simulations. Assuming that the Onsager relation holds, the viscous coupling parameters are $R_{23}=R_{32}=0.77\times10^8$ kg m^{-3} s^{-1} and $R_{41}=R_{14}=0.77\times10^8$ kg m^{-3} s^{-1}. The magnitudes of R_{24} and R_{42} have almost no impact on the solutions presented here and are chosen to be $R_{24}=R_{42}=0.77\times10^8$ kg m^{-3} s^{-1}. The characteristic time for raising the column is $\tau_r=10^4$ s=2 h, 46 min, 40 s.

V. SIMULATION RESULTS

Three laboratory experiments on a closed column have been simulated. The results are reported in this section. The three experiments differ in the way the column is moved in a gravitational field, in particular how the angle ϑ of the column toward gravity changes with time. We emphasize again that the results presented here are approximate. Although the algorithm discussed above has been extensively tested on many problems [50] its accuracy cannot be guaranteed for the problem at hand.

A. Simulation 1: Raising a closed column

In the first simulation the closed column is initially placed horizontally so that the angle ϑ between the column orientation and the direction perpendicular to gravity is zero, $\vartheta(0)=0$. The initial conditions for saturations, velocities, and pressure are those specified in column A in Table II. Because body forces and gradients of the stress tensors are absent the initial state is a stationary solution. The system could remain in its initial state forever. After the initial stationary state has been prepared the column is rotated to a vertical position following the protocol

$$\vartheta(t)=\arcsin\left\{\frac{1}{2}\left[\tanh\left(\frac{t}{\tau_r}-5\right)+1\right]\right\}, \tag{39}$$

for $0\le t\le 150\tau_r$. As the column is rotated gravity induces a flux inside the column. Water starts to flow downward and oil upward. Hence, an imbibition process takes place in the lower part of the column while a drainage process takes place in the upper part. Within the transition zone the process changes between imbibition and drainage as a function of time and position. In the region, where the column is imbibed, nonpercolating oil is produced by snap-off and breakup of ganglia. The saturation of nonpercolating water S_2 is reduced, because nonpercolating water coalesces with percolating water. In the drainage regions nonpercolating water is produced and the saturation S_3 of percolating oil increases. Simultaneous drainage and imbibition processes are generally difficult to simulate within the traditional theory because different capillary pressure and relative permeability functions have to be known and specified in advance. The present theory does not need any adjusting of such parameter functions because such process changes are intrinsically contained within it [56].

After the column has been raised the flow processes will eventually come to rest and the system reaches a new stationary state. In our simulation this happens after roughly $t\approx150\tau_r$. The resulting stationary saturation profiles are shown as solid curves in Fig. 1. The initial saturation profiles are represented as dotted vertical lines. The profiles show a clear separation of the imbibition and drainage zone. Note also that the numerical results show inflection points at $x\approx2.1$ m.

For comparison the quasistatic analytical solution obtained in [30] has been included into Fig. 1 as the dashed profiles. These were obtained from the same initial conditions as the numerical profiles. The two sets of profiles are clearly different. We attribute this difference to several factors. First, the quasistatic limit approximation assumes that the velocities of the percolating phases vanish. However, velocities up to $v_i\approx10^{-3}$ m/s occur during the approach to equilibrium and hence this assumption did not hold in our numerical simulation. Second, the analytical calculation does not need to consider the viscous resistance coefficients R_{ij}. In particular the difference between R_{25}, R_{45} and the other coefficients played no role. Third, the boundary conditions do not enter into the dynamics of the quasistatic calculation. Note that the quasistatic profiles show kinks at $x\approx2.4$ m instead of inflection points.

B. Simulation 2: Rotating a closed column upside down

In the second simulation the column is again initially oriented horizontally. The protocol for the angle ϑ is now

$$\vartheta(t)=\begin{cases}\arcsin\left\{\frac{1}{2}\left[\tanh\left(\frac{t}{\tau_r}-5\right)+1\right]\right\}, & t<50\tau_r\\ \arcsin\left[-\tanh\left(\frac{t}{\tau_r}-105\right)\right], & 50\tau_r\le t<150\tau_r\\ \arcsin\left[\tanh\left(\frac{t}{\tau_r}-205\right)\right], & t\ge150\tau_r.\end{cases} \tag{40}$$

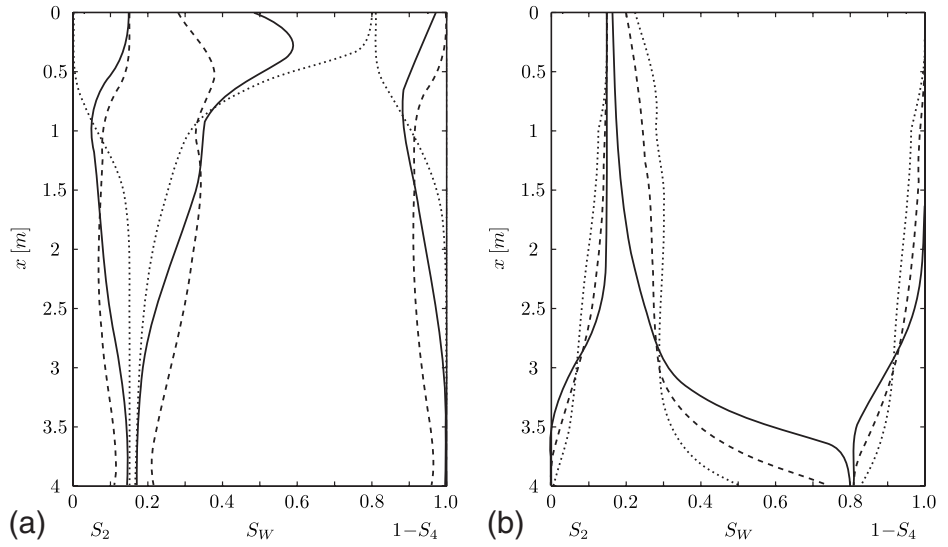

FIG. 3. Transient saturation profiles in simulation 2 after the second rotation of the column. (a) shows profiles at $t=200\tau_r$ (dotted curves), $t=208\tau_r$ (solid curves), and $t=210\tau_r$ (dashed curves). (b) shows profiles at $t=214.5\tau_r$ (dashed curves), $t=219\tau_r$ (solid curves), and $t=300\tau_r$ (dotted curves).

After the preparation, the column is first rotated to a vertical orientation as in simulation 1. This is represented by the first line in Eq. (40). Next one waits for the sample to reach a stationary state until time $t\approx 100\tau_r$ as seen in the second line of Eq. (40). Then the sample is rotated upside down by 180°. Again the system is given time to reach a stationary state until $t\approx 200\tau_r$ at which point it is rotated again by 180°.

Simulation 2 was carried out with this protocol for two different initial conditions. The two initial conditions are those specified in columns D and E of Table II. For both initial conditions the total water content was only 30%, not 50% as in simulation 1. As a consequence the stationary state is reached faster than in simulation 1 and it suffices to wait until $t=100\tau_r$ for the first rotation to start.

The results for both initial conditions are summarized in Fig. 2. Figure 2(a) shows the stationary profiles reached after raising the column from horizontal to vertical, while Fig. 2(b) shows the profiles reached at the end of the simulation. Solid curves are the profiles corresponding to initial condition D. Dashed curves represent saturation profiles corresponding to initial condition E. The dashed curves in Fig. 2(b) are not visible because they coincide with the solid curves. Initial saturation profiles are shown as dashed-dotted vertical straight lines in Fig. 2(a) for case D, while initial conditions E are shown as dotted lines. Note that the vertical line at $S_{\mathbb{W}}=0.3$ is a superposition of dotted and dashed-dotted lines. Note also that there is a dotted vertical line at $1-S_4=0.999$ and a dashed-dotted line at $S_2=0.001$. The stationary (solid and dashed) curves in Fig. 2(a) become the initial conditions for the twofold rotation by 180° illustrated in Fig. 2(b). Thus, the solid and dashed curves in Fig. 2(a) are identical with the dashed-dotted and dotted curves in Fig. 2(b).

Figure 2(a) shows first and foremost that the stationary profiles depend sensitively on the initial conditions for the nonpercolating phases. Initial conditions D and E both have $S_{\mathbb{W}}=0.3$ and are indistinguishable within the traditional theory. Consequently, the traditional theory would predict the same result for both types of initial conditions. In case D nonpercolating water is produced while it is annihilated in case E. Similarly, in case D nonpercolating oil is annihilated while percolating oil is produced. Figure 2(a) shows also that the total amount of nonpercolating fluids left after a displacement process can be very different depending on their initial distributions.

Figure 2(b) illustrates that multiple rotations by 180° ultimately result in a saturation profile that is a combination of a simple imbibition profile in the lower part and a simple drainage profile in the upper part. In other words the resulting profile (represented by the solid and superposed dotted curves) may be viewed as a kind of hybrid capillary pressure curve. Near the upper boundary the process is always a drainage while it is always an imbibition process near the lower boundary.

Figure 3 shows the time evolution of the saturation profiles from $t=200\tau_r$ to $t=300\tau_r$. To avoid overcrowding the figure the six time instants are shown in Figs. 3(a) and 3(b). As the amount of water decreases in the region $0\ \mathrm{m}\leq x\leq 1\ \mathrm{m}$, nonpercolating water is produced and nonpercolating oil is reduced significantly. In the lower part $(1\ \mathrm{m}\leq x\leq 4\ \mathrm{m})$ slight imbibition takes place, which results in a small increase in nonpercolating oil and a decrease in nonpercolating water. In Fig. 3(b), i.e., toward the end of the process, the imbibition takes place only in the lowest quarter $(3\ \mathrm{m}\leq x\leq 4\ \mathrm{m})$ of the column. The imbibition is complete in the sense that nonpercolating water is completely consumed and oil remains only as nonpercolating oil. In the upper part of the column $(0\ \mathrm{m}\leq x\leq 3\ \mathrm{m})$ a drainage process increases nonpercolating water and decreases nonpercolating oil. We emphasize that in the middle region drainage and imbibition occur consecutively at a given position. This poses a difficult problem within the traditional theory for two reasons. First, it requires the specification of multiple capillary pressure and relative permeability curves in advance without experimental

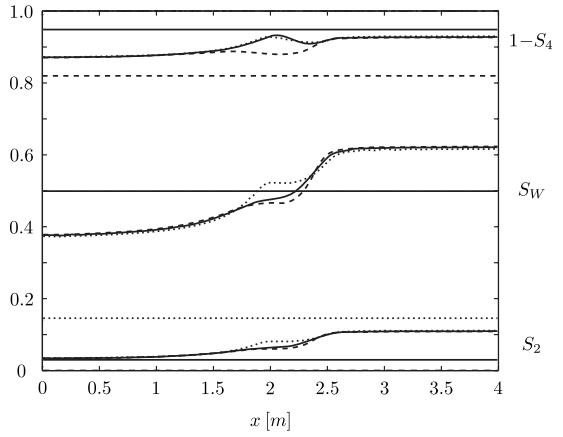

FIG. 4. Initial and final saturation profiles for simulation 3. Straight lines are initial profiles while curves are final profiles. Three simulations are shown corresponding to the initial conditions of columns A (solid line), B (dotted line), and C (dashed line) in Table II. Note that there is a dashed line at $S_2=0.001$, a dotted line at $1-S_4=0.999$, and the solid line at $S_{\mathbb{W}}=0.5$ coincides with a dashed and a dotted line.

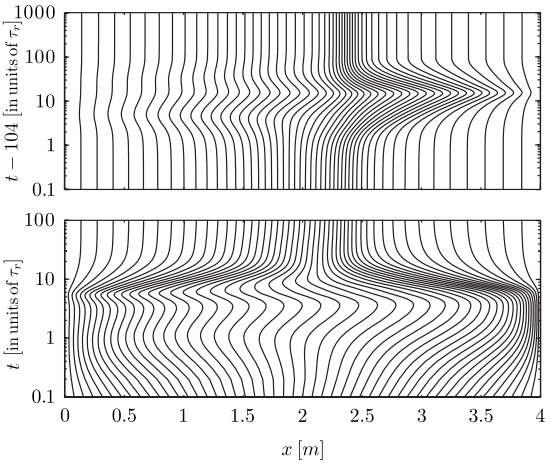

FIG. 5. Trajectories of the grid points during the raising of a closed column in a gravitational field and lowering it again for the initial conditions of type A. The time axis is scaled logarithmically. For the upper graph the plot is shifted by $t_0=104\tau_r$ to better depict the dynamics after lowering the column.

knowledge and second it leads to computationally cumbersome case selections.

C. Simulation 3: Raising and lowering a closed column

As in the previous simulations the column is first raised from a horizontal to a vertical position. After reaching a stationary profile around $t\approx 100\tau_r$ the column is rotated back to its initial horizontal position. The final stationary state is reached at $t\approx 200\tau_r$. The protocol for simulation 3 is

$$\vartheta(t)=\begin{cases}\arcsin\left\{\frac{1}{2}\left[1+\tanh\left(\frac{t}{\tau_r}-5\right)\right]\right\}, & t<50\tau_r\\ \arcsin\left\{\frac{1}{2}\left[1-\tanh\left(\frac{t}{\tau_r}-105\right)\right]\right\}, & t\geq 50\tau_r.\end{cases} \tag{41}$$

Simulation 3 was carried out with this protocol for three different initial conditions. The three initial conditions are those specified in columns A–C of Table II. For all initial conditions the water content was 50%.

The final stationary profiles for all three initial conditions are summarized in Fig. 4. Solid curves show the final profiles for case A, dotted curves for case B, and dashed curves for case C. The corresponding initial conditions are depicted by straight lines of the same style. Note that the line $S_{\mathbb{W}}=0.5$ is a triple curve because in all three initial conditions the column is filled with 50% water. Note also that there is a dashed line at $S_2=0.001$ and a dotted line at $1-S_4=0.999$.

Figure 4 shows that the final profiles are not constant. This contrasts with the traditional theory where $S_{\mathbb{W}}=S_{\mathbb{O}}=0.5$ for all x would be the final stationary result. Irreversible hysteretic switching between different flow processes in the present theory prevents the system to return to its original state. The fluids come to rest before the nonpercolating phases can return to their initial amount. A stationary profile is reached showing the same separation into a drainage dominated zone on the left and an imbibition dominated zone on the right. The two zones are separated by a transition zone characterized by temporal switching between imbibition and drainage. Nonmonotonous nonpercolating saturations are observed in this transition zone. If the raising and lowering of the column is repeated several times the profiles approach a limiting profile. These observations resemble the observations made in simulation 2.

The solid line in Fig. 4 corresponds to the same initial conditions (type A) that were used also for the solid profiles in Fig. 1. Combined with the observations in the other two simulations this highlights the large degeneracy of equilibrium saturation profiles (i.e., profiles for $v_i=0$).

To illustrate the time evolution of the saturations and the adaptivity of the algorithm the trajectories of the grid points are shown in Fig. 5. Because the grid points assemble near large gradients, a high density of trajectories indicates a saturation front. The time scale is logarithmic because saturation fronts start to move rapidly through the column when the column orientation is changed. They slow down strongly as they approach the stationary profiles. The plot of the upper graph is shifted by $t_0=104\tau_r$ to better visualize the dynamics after the column has been lowered again.

At the beginning the saturation profiles are homogeneous and the grid points are distributed equidistantly through the whole domain. As the column is raised a water front is moving from the bottom of the column toward the center of the column and an oil front is moving down from the top until both fronts meet in the middle. Due to the wetting properties of the two fluids the water front is steeper. This results in a higher density of grid points in the range $2\ \mathrm{m}\leq x\leq 4\ \mathrm{m}$, $t\approx 5\tau_r$. At $t\approx 20\tau_r$ the stationary profile (the same as the solid lines in Fig. 1) is almost reached and the grid points do not move anymore. When the column is lowered down again ($t\approx 1.05\tau_r$) the two fronts move back again. After reaching the boundaries the gradients in the saturations are reduced by capillary diffusion. Finally, only the step at $x\approx 2.5\ \mathrm{m}$ (com-

pare with solid curves in Fig. 4) remains, which results in an accumulation of the grid points at that position.

VI. CONCLUSION

Numerically approximate but convergent solutions were found for a recent mathematical model for multiphase flow in porous media, which takes into account the difference of percolating and nonpercolating, trapped or immobile fluid regions. The system of equations was closed self-consistently by the capillary pressure-saturation relation, which was obtained as an output of the residual decoupling approximation already in [40]. Displacement processes with simultaneous drainage and imbibition can be simulated without difficulty in contrast to the widely used traditional theory. Initial and boundary value problems for raising and lowering a closed column in a gravitational field were used as illustrations. The initial and boundary value problems can be realized in experiments and can be used to test the extended theory. The theory predicts the spatial distribution of trapped blobs and ganglia after a water flood. The results exhibit irreversibility and hysteresis as expected from experiment.

ACKNOWLEDGMENTS

The authors gratefully acknowledge financial support from the Deutsche Forschungsgemeinschaft (DFG) and the International Research and Training Group on Nonlinearities and Upscaling in Porous Media (NUPUS). We thank an anonymous referee for thoughtful comments and suggestions to improve the manuscript.

[1] J. Jamin, Acad. Sci., Paris, C. R. **50**, 172 (1860).
[2] L. A. Richards, Physics **1**, 318 (1931).
[3] P. deGennes, EPL **5**, 689 (1988).
[4] R. Hilfer and P. Øren, Transp. Porous Media **22**, 53 (1996).
[5] L. Anton and R. Hilfer, Phys. Rev. E **59**, 6819 (1999).
[6] M. van Dijke and K. Sorbie, Phys. Rev. E **66**, 046302 (2002).
[7] M. Ferer, G. S. Bromhal, and D. H. Smith, Phys. Rev. E **67**, 051601 (2003).
[8] I. I. Bogdanov, V. V. Mourzenko, J. F. Thovert, and P. M. Adler, Phys. Rev. E **68**, 026703 (2003).
[9] M. Muskat and M. Meres, Physics (N.Y.) **7**, 346 (1936).
[10] R. Wyckoff and H. Botset, Physics (N.Y.) **7**, 325 (1936).
[11] M. Muskat, R. Wyckoff, H. Botset, and M. Meres, Trans. AIME **123**, 69 (1937).
[12] M. Leverett, Trans. AIME **142**, 152 (1941).
[13] A. Scheidegger, *The Physics of Flow Through Porous Media* (University of Toronto Press, Canada, 1957).
[14] J. Bear, *Dynamics of Fluids in Porous Media* (Elsevier, New York, 1972).
[15] F. Dullien, *Porous Media—Fluid Transport and Pore Structure* (Academic, San Diego, CA, 1992).
[16] E. Donaldson, R. Thomas, and P. Lorenz, Soc. Pet. Eng. J. **9**, 13 (1969).
[17] W. England, A. Mackenzie, D. Mann, and T. Quigley, J. Geol. Soc. (London) **144**, 327 (1987).
[18] K. Wu, M. Dijke, G. Couples, Z. Jiang, J. Ma, K. Sorbie, J. Crawford, I. Young, and X. Zhang, Transp. Porous Media **65**, 443 (2006).
[19] Z. Zhang and J. Smith, Transp. Porous Media **48**, 41 (2002).
[20] A. Ebigbo, H. Class, and R. Helmig, Comput. Geosci. **11**, 103 (2007).
[21] M. Kataja, K. Hiltunen, and J. Timonen, J. Phys. D **25**, 1053 (1992).
[22] U. Pasaogullari and C. Wang, J. Electrochem. Soc. **151**, A399 (2004).
[23] A. Babchin, I. Brailovsky, P. Gordon, and G. Sivashinsky, Phys. Rev. E **77**, 026301 (2008).
[24] M. R. Deinert, A. Dathe, J. Y. Parlange, and K. B. Cady, Phys. Rev. E **77**, 021203 (2008).
[25] P. Lehmann, S. Assouline, and D. Or, Phys. Rev. E **77**, 056309 (2008).
[26] S. Naumov, A. Khokhlov, R. Valiullin, J. Kärger, and P. A. Monson, Phys. Rev. E **78**, 060601(R) (2008).
[27] L. Cueto-Felgueroso and R. Juanes, Phys. Rev. Lett. **101**, 244504 (2008).
[28] R. Hilfer, Adv. Chem. Phys. **92**, 299 (1996).
[29] R. Hilfer, Phys. Rev. E **73**, 016307 (2006).
[30] R. Hilfer, Physica A **371**, 209 (2006).
[31] N. Morrow, in *Interfacial Phenomena in Petroleum Recovery*, edited by N. Morrow, Surfactant Science Series Vol. 36 (Dekker, New York, 1991), p. 1.
[32] Y. Mualem, Water Resour. Res. **9**, 1324 (1973).
[33] J. Kloubek, J. Adhes. Sci. Technol. **6**, 667 (1992).
[34] A. Abrams, Soc. Pet. Eng. J. **15**, 437 (1975).
[35] P. Sheng and M. Zhou, Phys. Rev. A **45**, 5694 (1992).
[36] S. Hassanizadeh, M. Celia, and H. Dahle, Vadose Zone J. **1**, 38 (2002).
[37] C. Tsakiroglou, D. Avraam, and A. Payatakes, Adv. Water Resour. **30**, 1981 (2007).
[38] C. Marle, Int. J. Eng. Sci. **20**, 643 (1982).
[39] D. G. Avraam and A. C. Payatakes, Transp. Porous Media **20**, 135 (1995).
[40] R. Hilfer, Physica A **359**, 119 (2006).
[41] R. Hilfer, in *CP1091, Modeling and Simulation of Materials*, edited by P. Garrido, P. Hurtado, and J. Marro (AIP, New York, 2009), p. 141.
[42] R. Hilfer, Phys. Rev. E **58**, 2090 (1998).
[43] R. Hilfer and H. Besserer, Physica B **279**, 125 (2000).
[44] J. Blom and P. Zegeling, ACM Trans. Math. Softw. **20**, 194 (1994).
[45] P. Zegeling, I. Lagzi, and F. Izsak (unpublished).
[46] B. Ataie-Ashtiani, S. Hassanizadeh, O. Oung, F. Westrate, and A. Bezuijen, Environ. Modell. Software **18**, 231 (2003).
[47] L. Petzold, Sandia National Laboratories Technical Report No. SAND82-8637, 1982 (unpublished).
[48] A. van Dam and P. Zegeling, J. Comput. Phys. **216**, 526 (2006).
[49] P. Zegeling, J. Comput. Appl. Math. **166**, 343 (2004).

[50] P. Zegeling, in *Adaptive Computations: Theory and Algorithms*, edited by T. Tang and J. Xu (Science, Peking, 2007), p. 251.
[51] K. Aziz and A. Settari, *Petroleum Reservoir Simulation* (Applied Science, London, 1979).
[52] R. Helmig, *Multiphase Flow and Transport Processes in the Subsurface* (Springer, Berlin, 1997).
[53] A. Chorin, J. Comput. Phys. **2**, 12 (1967).
[54] R. Rannacher, in *The Navier-Stokes Equation II—Theory and Numerical Methods*, edited by J. Heywood, K. Masuda, R. Rautmann, and V. Solonnikov (Springer Verlag, Berlin, 1992), pp. 167–183.
[55] J. Shen, in *Advances in Computer Methods for Partial Differential Equations*, edited by R. Vichnevestsky, D. Knight, and G. Richter (International Association for Mathematics and Computers in Simulation, New Brunswick, 1992), p. 658.
[56] R. Hilfer and F. Doster, Trans. Porous Media (2009), doi: 10.1007/s11242-009-9395-0